

# Effects of Damage Evolution on Edge Crack Sensitivity in Dual-Phase Steels

Niloufar Habibi,\* Thorsten Beier, Junhe Lian, Berk Tekkaya, Markus Koenemann, and Sebastian Muenstermann

The present study aims to thoroughly investigate the edge-cracking phenomenon in high-strength sheets. Hence, the edge crack sensitivity of three dual-phase steels is studied in various combinations of edge manufacturing and forming processes. Finite element simulations are performed to elaborate the study. In this regard, the Yoshida–Uemori kinematic hardening model is employed to describe the plasticity behavior of the materials under multistep processes. A stress-state fracture model is coupled with this plasticity model to illustrate the distinguished local fracture strains of each material. Moreover, the effects of strain rate and the consequent temperature rise on hardening and damage are taken into account, which play significant roles during shear-cutting. The results show that although the shear-cutting processes are applied at very low speed, the strain rate and induced temperature are still high at the cutting area. The hole expansion results show different fracture behaviors for different cases. In brief, cracking is initiated at a location, which shows the highest damage accumulation during edge manufacturing plus the subsequent forming process. Such a complicated situation can only be successfully predicted by using a computer-aided approach along with proper material modeling, like the applied model in this study.

## 1. Introduction


The hostile global environmental and economic situations have compelled automotive manufacturers to develop lightweight components that meet stringent crash safety requirements.<sup>[1]</sup> In this pursuit, the continuous design and improvement of new advanced materials, such as dual-phase (DP) steels, aim to achieve an optimal balance between strength and formability. However, the complex multistep forming processes involved in creating the final product trigger several problems that hinder the widespread application of these materials. One of the unresolved challenges in sheet forming of high-strength materials is edge cracking, which appears despite conventional forming limits anticipating further deformation as a safe condition.<sup>[2]</sup> To overcome this problem, there is a need for new damage evaluation methods that rely on a deep understanding of this phenomenon to successfully design highly efficient forming procedures.

Casellas et al.<sup>[3]</sup> conducted experiments to measure the hole expansion ratios (HER) of various advanced high-strength steel sheets as a quantitative factor of edge crack sensitivity. Their HER results exhibited a similar trend as the materials' essential work of fracture. Heibel et al.<sup>[4]</sup> showed the relationship between HER and local formability, which was defined by true thickness strain at fracture. Although these methods were successful in the studied cases, they should be verified under different stress states as well, since the cutting and subsequent forming processes are significantly influenced by loading modes. Therefore, employing hybrid testing and simulation methods could be a promising choice for considering various conditions even for various scales.<sup>[5]</sup> Complex microstructure in multiphase steels causes different local formability behaviors and consequently edge crack sensitivity.<sup>[6–9]</sup> Namely, phase fraction, phase distribution, texture, individual morphological characteristics, and mechanical behavior of each phase could change the local formability of the materials. The role of these features has also been investigated through numerical approaches using representative volume element models along with finite element (FE) simulations.<sup>[10,11]</sup> These studies collectively suggest that a homogeneous strain distribution throughout the material can enhance local formability under various loading conditions.

N. Habibi, B. Tekkaya, M. Koenemann, S. Muenstermann  
Institute of Metal Forming  
RWTH Aachen University  
Intzestraße 10, 52072 Aachen, Germany  
E-mail: niloufar.habibi@ibf.rwth-aachen.de

T. Beier  
Thyssenkrupp Steel Europe AG  
Kaiser-Wilhelm-Str. 100, 47166 Duisburg, Germany

J. Lian  
Advanced Materials and Manufacturing  
Department of Mechanical Engineering  
Aalto University  
Puumiehenkuja 3, 02150 Espoo, Finland

 The ORCID identification number(s) for the author(s) of this article can be found under <https://doi.org/10.1002/srin.202400178>.

© 2024 The Author(s). Steel Research International published by Wiley-VCH GmbH. This is an open access article under the terms of the Creative Commons Attribution-NonCommercial-NoDerivs License, which permits use and distribution in any medium, provided the original work is properly cited, the use is non-commercial and no modifications or adaptations are made.

DOI: 10.1002/srin.202400178

In addition to the materials' intrinsic properties, the tooling design plays a critical role in exacerbating the issue of edge-forming limitation. It encompasses the manufacturing technique utilized for edge creation and subsequent edge-forming processes. Punching is widely employed as an initial manufacturing process in the industry due to its great cost-effectiveness and efficiency. However, it applies severe hardening and damage to the shear-affected zone (SAZ). Consequently, a rough low-quality edge is produced, which facilitates premature failure from the edge. Wang et al.<sup>[12]</sup> have documented considerable dissimilarities in the HER of DP780 steel across varying hole expansion tests (HET). Their findings demonstrated HER of 38% and 35% for milled and waterjet cut holes, whereas 12% for the punched holes. In addition, the relationship between clearance and HER has garnered significant attention and various studies tried to unravel underlying mechanisms and optimize hole expansion performance.<sup>[13–15]</sup> The clearance parameter directly impacts materials' flow and deformation behavior during plastic deformation. A larger clearance expands SAZ and produces a larger burr, which leads to higher edge cracking sensitivity. On the other hand, narrow clearance could also cause a secondary burnish which reduces HER. Wu et al.<sup>[16]</sup> argued a narrow clearance could suppress the main crack to develop throughout the thickness. Therefore, a secondary shearing and multiple microcracks form to separate the remaining thickness. These microcracks create rougher surfaces and lower edge quality.<sup>[17]</sup>

Moreover, the influences of hole expansion punches with different shapes have been investigated. Wang et al.<sup>[12]</sup> showed conical, flat, and spherical punches apply different contact conditions and strain gradients. Conical punches maximize edge stretching, causing specimen rotation and nonuniform strain distributions. Flat punches cause minimal rotation near the edge leading to edge cracks occurring away from it. Spherical punches offer an intermediate loading condition with moderate strain gradients. Paul<sup>[18]</sup> observed that failure initiation occurs at the hole edge when employing a conical punch. However, in the case of hemispherical and flat-bottom punches, failure initiation was found to occur slightly away from that, that is, inside of the sheet rather than at the edge. Krempaszky et al.<sup>[19]</sup> concluded that higher contact pressure, resulting from a smaller initial hole size and a smaller cone angle of the hole expansion punch, facilitates local necking formation. This phenomenon plays a key role in significant HER reduction. The explanation for this behavior lies in the concept of applied strain gradient.<sup>[18,20]</sup> The presence of higher strain gradients suppresses plain strain necking at the punch-sheet contact site and allows edge cracking to happen.

Prediction of various edge manufacturing and following forming processes requires a powerful numerical tool to consider the effects of stress states, strain rates, adiabatic heating, and probable Bauschinger effect on hardening and damage behaviors. This study aims to propose a computer-aided approach to take all the aforementioned factors into account, unlike the existing studies which considered only part of them at the same time. In addition, its accuracy was verified successfully for different materials under various edgcutting and forming procedures.

## 2. Experimental Section

### 2.1. Materials

For this work, three different dual-phase (DP) steel sheets were studied with a thickness of 1.5 mm, and the commercial names were CR440Y780T-DP, CR590Y980T-DP, and CR700Y980T-DP. In these names, the first number addressed the yield stress and the second number stood for the ultimate tensile strength. The chemical compositions are listed in **Table 1** and their as-received microstructures are shown in **Figure 1**. All the microstructures consisted of ferrite and martensite phases. The phase fractions were calculated using Digimizer image analysis for several scanning electron microscope (SEM) images, while the relatively lighter and darker phases were marked as martensite and ferrite, respectively. To evaluate strength differences between the phases, the carbon contents were measured by electron probe microanalysis (EPMA) as 15  $\mu\text{m}$  line scans of the microstructures.

### 2.2. Experimental Procedure

#### 2.2.1. Experiments for Calibration of the Models

The plasticity model was calibrated using cyclic in-plane torsion tests, which were described in another study.<sup>[21]</sup> Furthermore, the effects of a wide range of stress states on damage behavior were investigated for each material. In this regard, various testing methods were applied, including monotonic in-plane torsion, bulge, tensile tests with different notch geometries, and plane-strain tests, as shown in **Figure 2**. For detailed information about the technical drawings of specimens and experimental results, see ref. [8]. Furthermore, SEM was used to investigate the fracture surface and damage micromechanisms.

#### 2.2.2. Shear-Cutting and Subsequent HET

In order to study the edge crack sensitivity, several edge conditions were manufactured through shear-cutting process and expanded with a conical or flat-bottom punch according to ISO 16 630:2017.<sup>[22]</sup> The tool conditions for each step are summarized in **Table 2** and the speed of punches in both steps was  $1 \text{ mm s}^{-1}$ . The HER were measured as a quantitative parameter of edge cracking sensitivity. According to the aforementioned standard, HER should be calculated as a through-thickness edge crack occurred.

This evaluation was assisted by video recording techniques which allowed precise results to be extracted. Note that

**Table 1.** Chemical composition of the studied DP steels.

	C	Si	Mn	Al	Cr	Mo	Cu	Ti
DP440/780	0.149	0.212	1.670	0.049	0.733	0.011	0.044	0.031
DP590/980	0.074	0.301	1.830	0.048	0.387	0.061	0.023	0.048
	0.043	0.301	1.807	0.037	0.380	0.063	0.022	0.048
DP700/980	0.074	0.294	2.498	0.037	0.693	0.118	0.123	0.076
	0.080	0.293	2.813	0.291	0.689	0.119	0.121	0.075

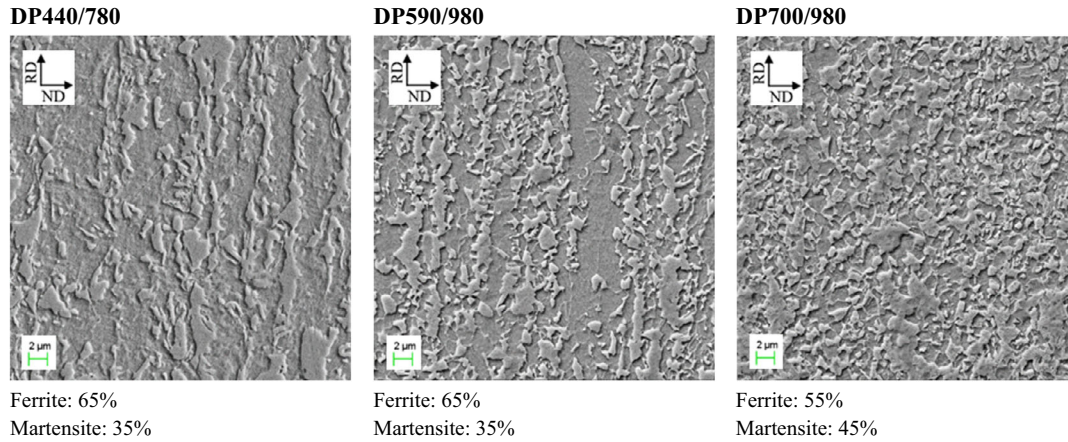


**Figure 1.** The initial microstructure and phase fraction for the studied materials.

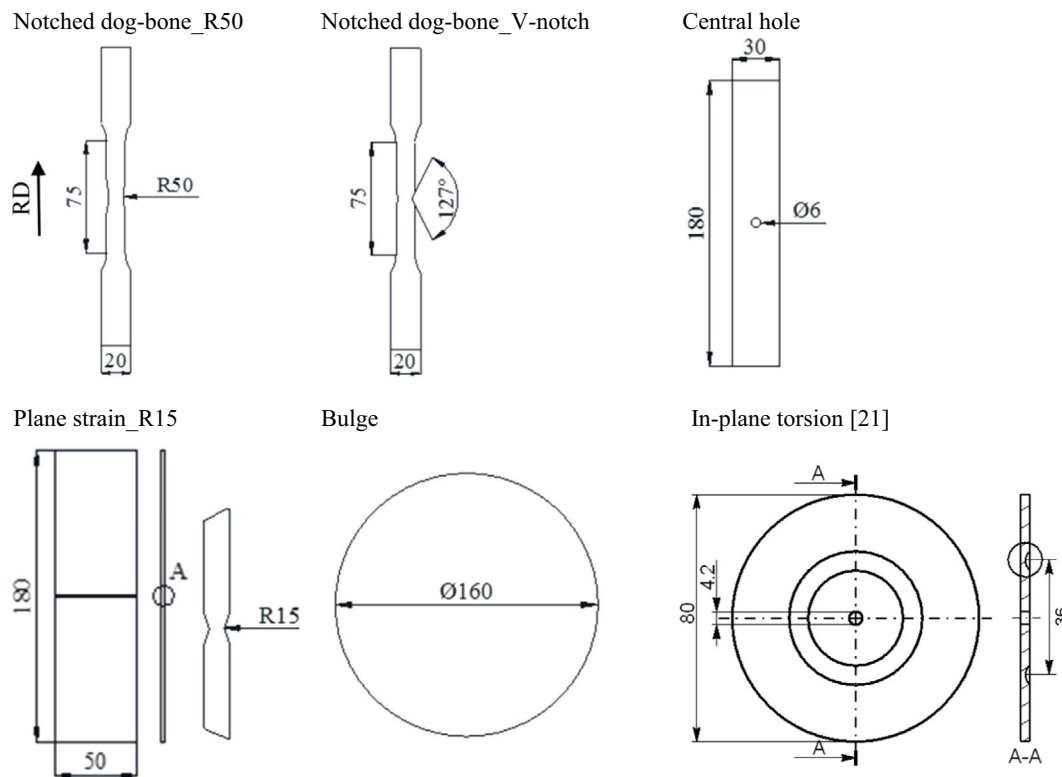


**Figure 2.** The specimen geometries of applied tests.

similar hole sizes were manufactured by wire-cutting as well to compare the potential of edge formability regarding predamage effects.

## 2.3. Numerical Procedure

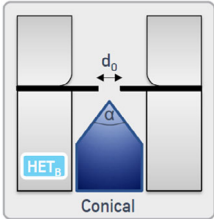
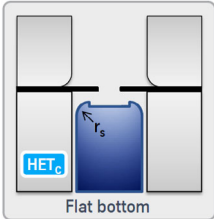
### 2.3.1. Material Model

Since the materials underwent complex multistep deformation processes, that is, shear-cutting followed by HET, changes in

the yield stress should be considered. Therefore, a nonlinear kinematic hardening model was used to describe the plasticity behavior more precisely. The damage behavior was also modeled using a stress state-dependent phenomenological damage criterion which was coupled with the plasticity model. The models and implementation method were explained in the following. Note that all bold symbols showed tensor variables and the rest were scalar variables.

**Plasticity and Yielding Models:** The general yielding function ( $\Phi$ ) was described in stress space as follows

**Table 2.** Tool conditions of used cutting and hole expansion processes.

Shear-cutting tool			Hole expansion tool	
Ø Die	Ø Punch	Clearance	Conical 50° Ø 100 mm	Flat-bottom Ø 100 mm; $R_s 15$
30 mm	29.7 mm	10.0%		
	29.6 mm	13.3%		
39.97 mm	39.67 mm	10.0%		
	39.57 mm	13.3%		

$$\Phi = \bar{\sigma} - \sigma_Y = 0 \quad (1)$$

$\bar{\sigma}$  is equivalent stress and calculated according to von Mises yield criterion ( $\bar{\sigma}_{VM}$ ) (Equation (2))

$$\bar{\sigma} = \bar{\sigma}_{VM} = \sqrt{\frac{3}{2}} \|s - \alpha\| \quad (2)$$

where  $s$  and  $\alpha$  are deviatoric stress tensor and back stress tensor, respectively.  $\sigma_Y$  is yield stress. Since the strain rate could be high especially during shear-cutting and generate adiabatic heating, a multiplied function was used for yield stress calculation (Equation (3))

$$\sigma_Y = \sigma_{Y(\dot{\epsilon}^P, \dot{\epsilon}_0^P, T_0)} \cdot \sigma_{Y(\dot{\epsilon}^P)} \cdot \sigma_{Y(T)} \quad (3)$$

$\sigma_{Y(\dot{\epsilon}^P, \dot{\epsilon}_0^P, T_0)}$  showed the stress–strain curve under the reference strain rate ( $\dot{\epsilon}_0^P$ ) and temperature ( $T_0$ ). The strain rate and temperature correction function are defined in Equation (4) and (5), respectively

$$\sigma_{Y(\dot{\epsilon}^P)} = c_1^{\dot{\epsilon}^P} \cdot \ln \dot{\epsilon}^P + c_2^{\dot{\epsilon}^P} \quad (4)$$

$$\sigma_{Y(T)} = c_1^T \cdot \exp(-c_2^T \cdot T) + c_3^T \quad (5)$$

The temperature changes ( $\Delta T$ ) due to adiabatic heating could be calculated in Equation (6)<sup>[23,24]</sup>

$$\Delta T = \frac{\beta_{TQ}}{\rho \cdot C_p} \cdot \sigma_Y \cdot \Delta \epsilon^P \quad (6)$$

where  $\beta_{TQ}$  is Taylor–Quinney coefficient,  $\rho$  is density, and  $C_p$  is specific heat capacity. They were all material dependent. The increment of plastic strain ( $\Delta \epsilon^P$ ) was determined by applying the associated flow rule in the following equation

$$\Delta \epsilon^P = \Delta \gamma n \quad (7)$$

where  $n$  is the normal yield surface and is  $\gamma$  effective plastic strain.

The Yoshida–Uemori (YU) two-surface plasticity model<sup>[25]</sup> was employed in this work to satisfy the multistep deformation requirements for capturing the Bauschinger effect. It contained two surfaces, the yield surface (the inner one) with the radius of  $Y$

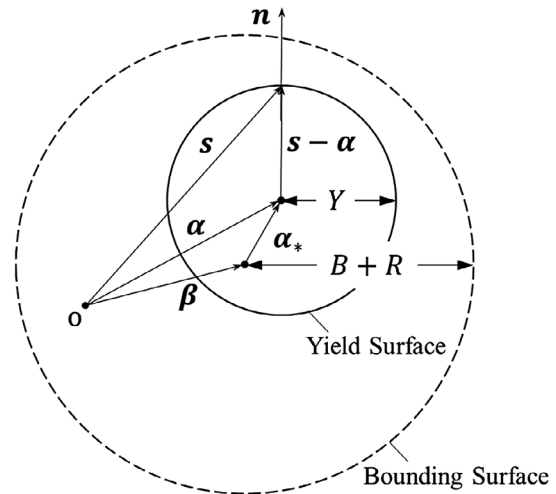


**Figure 3.** Schematic illustration of the YU model. Reproduced with permission.<sup>[25]</sup> Copyright 2002, Elsevier.

and the bounding surface (the outer one) with the radius of  $B + R$  (Figure 3). The yield surface represented the plastic deformation occurrence by translating across the bounding surface while its size remained constant ( $Y$ ), therefore

$$\sigma_{Y(\dot{\epsilon}^P, \dot{\epsilon}_0^P, T_0)} = Y \quad (8)$$

whereas the bounding surface was able to both move and expand. The evolution of the yield surface is as follows

$$\dot{\alpha} = \dot{\beta} + \dot{\alpha}_* \quad (9)$$

where  $\dot{\beta}$  is the kinematic hardening rate of the bounding surface

$$\dot{\beta} = k \left( \frac{b}{Y} (s - \alpha) - \beta \right) \dot{\gamma} \quad (10)$$

and  $\dot{\alpha}_*$  is the relative kinematic motion

$$\dot{\alpha}_* = C \left( \frac{B + R - Y}{Y} (s - \alpha) - \sqrt{\frac{B + R - Y}{\alpha_*}} \alpha_* \right) \dot{\gamma} \quad (11)$$



$C$ ,  $B$ , and  $Y$  are material constants.  $R$  is the nonlinear isotropic hardening component of bounding surface and it evolves as follows

$$\dot{R} = k(R_{\text{sat}} - R) \dot{\gamma} \quad (12)$$

$k$  and  $R$  are material constants.

**Damage Evolution Model:** A strain-based phenomenological ductile damage criterion was used to describe damage initiation, propagation, and fracture. The range of each stage was determined by two indicators,  $I_{\text{ddi}}$  and  $I_{\text{df}}$  in damage parameter ( $D$ ) (Equation 13). The indicators calculated the accumulation of damage throughout nonproportional loading paths and considered the stress state at each increment as stress triaxiality ( $\eta$ ) and normalized Lode angle parameter ( $\bar{\theta}$ ) (Equation (14)–(17)). Note that the relation between damage initiation and fracture strains with loading condition was defined using the Bai–Wierzbicki (BW) model.<sup>[26–28]</sup> A more detailed description of the model can be found in the previous study.<sup>[29]</sup> Parameters  $\sigma_{\text{ddi}}^c$ ,  $G_f$ ,  $C_i$ , and  $D_i$  were material constants. It was noted that a changeable cutoff value for damage was considered in this study as  $\eta_c < -\frac{3-\bar{\theta}}{3\sqrt{\bar{\theta}^2+3}} + 1/3$ , which was proposed for a DP980 steel.<sup>[30]</sup> Therefore, no damage would accumulate in the case  $\eta < \eta_c$

$$D = \begin{cases} 0 & I_{\text{ddi}} < 1 \\ \frac{\sigma_{\text{ddi}}^c}{G_f} \int_{\epsilon_{\text{di}}^p}^{\epsilon^p} d\epsilon^p & I_{\text{ddi}} \geq 1 \wedge I_{\text{df}} < 1 \\ 1 & I_{\text{ddi}} \geq 1 \wedge I_{\text{df}} \geq 1 \end{cases} \quad (13)$$

$$I_{\text{ddi}} = \int_0^{\epsilon^p} \frac{d\epsilon^p}{\epsilon_{\text{ddi}}^p(\eta, \bar{\theta})} \quad (14)$$

$$\text{where } \epsilon_{\text{ddi}}^p(\eta, \bar{\theta}) = \begin{cases} +\infty & \eta \leq \eta_c \\ f_{\text{ddi}}(\eta, \bar{\theta}) & \eta > \eta_c \end{cases}$$

$$f_{\text{ddi}}(\eta, \bar{\theta}) = \left( \frac{1}{2} (C_1 e^{-C_2 \eta} + C_5 e^{-C_6 \eta}) - C_3 e^{-C_4 \eta} \right) \bar{\theta}^2 + \frac{1}{2} (C_1 e^{-C_2 \eta} - C_5 e^{-C_6 \eta}) \bar{\theta} + C_3 e^{-C_4 \eta} \quad (15)$$

$$I_{\text{df}} = \int_{\epsilon_{\text{di}}^p}^{\epsilon^p} \frac{d\epsilon^p}{\epsilon_{\text{df}}^p(\eta, \bar{\theta}) - \epsilon_{\text{ddi}}^p(\eta, \bar{\theta})} \quad (16)$$

$$\text{where } \epsilon_{\text{df}}^p(\eta, \bar{\theta}) = \begin{cases} +\infty & \eta \leq \eta_c \\ f_{\text{df}}(\eta, \bar{\theta}) & \eta > \eta_c \end{cases}$$

$$f_{\text{df}}(\eta, \bar{\theta}) = \left( \frac{1}{2} (D_1 e^{-D_2 \eta} + D_5 e^{-D_6 \eta}) - D_3 e^{-D_4 \eta} \right) \bar{\theta}^2 + \frac{1}{2} (D_1 e^{-D_2 \eta} - D_5 e^{-D_6 \eta}) \bar{\theta} + D_3 e^{-D_4 \eta} \quad (17)$$

**Implementation of Damage Model in the Plasticity Model:** The plasticity model was coupled with the damage model through a user-defined VUMAT subroutine to use in Abaqus FE software, as described in the following. Note that the crack initiation and propagation were defined by element deletion.

In the FE context, for the time  $n$ , the current state variables were known, such as  $\epsilon_n^p$ ,  $\epsilon_n^p$ ,  $\sigma_n$ ,  $\alpha_n$ ,  $\beta_n$ ,  $\alpha_{*n}$ ,  $\bar{\sigma}_n$ , and  $D_n$ . For further plastic deformation at time step  $n+1$ , the plastic corrector/radial return mapping method was employed. In this regard, Hook's law is written as

$$\sigma_{n+1} = 2\mu \epsilon_{n+1}^e + \lambda \text{Tr}(\epsilon_{n+1}^e) I \quad (18)$$

where  $\mu$  and  $\lambda$  are the shear and Lamé moduli, respectively. The elastic strain at this time is

$$\epsilon_{n+1}^e = \epsilon_n^e + \Delta \epsilon^e \quad (19)$$

$$\Delta \epsilon^e = \Delta \epsilon - \Delta \epsilon^p \quad (20)$$

so that

$$\sigma_{n+1} = 2\mu(\epsilon_n^e + \Delta \epsilon - \Delta \epsilon^p) + \lambda \text{Tr}(\epsilon_n^e + \Delta \epsilon - \Delta \epsilon^p) I \quad (21)$$

Since

$$\text{Tr}(\Delta \epsilon^p) = 0 \quad (22)$$

The stress tensor could be written as [elastic predictor] – [plastic corrector]

$$\sigma_{n+1} = [2\mu(\epsilon_n^e + \Delta \epsilon) + \lambda \text{Tr}(\epsilon_n^e + \Delta \epsilon) I] - [2\mu \Delta \epsilon^p] \quad (23)$$

The elastic predictor or trial stress is

$$\sigma_{n+1}^{\text{trial}} = 2\mu(\epsilon_n^e + \Delta \epsilon) + \lambda \text{Tr}(\epsilon_n^e + \Delta \epsilon) I \quad (24)$$

The increment plastic strain tensor could be written according to the plastic multiplier and the plastic flow direction tensor

$$\Delta \epsilon^p = \Delta \gamma n_{n+1} \quad (25)$$

$$n_{n+1} = \frac{s_{n+1}^{\text{trial}} - \alpha_{n+1}}{\|s_{n+1}^{\text{trial}} - \alpha_{n+1}\|} = \frac{s_{n+1}^{\text{trial}} - \alpha_n}{\|s_{n+1}^{\text{trial}} - \alpha_n\|} \quad (26)$$

Thus, the stress tensor becomes

$$\sigma_{n+1} = \sigma_{n+1}^{\text{trial}} - 2\mu n_{n+1} \Delta \gamma \quad (27)$$

Then, the yielding possibility was checked considering the flow potential function as

$$\Phi_{n+1} = \bar{\sigma}_{n+1} - (1 - D_{n+1}) \sigma_Y = 0 \quad (28)$$

According to the aforementioned models and considering the von Mises yielding criterion, the description of each parameter would be

$$\bar{\sigma}_{n+1} = \sqrt{\frac{3}{2}} \|s_{n+1}^{\text{trial}} - (1 - D_{n+1}) \alpha_{n+1} - 2\mu n_{n+1} \Delta \gamma\| \quad (29)$$

$$\alpha_{n+1} = \alpha_n + \Delta \beta + \Delta \alpha_* \quad (30)$$

$$\Delta \beta = k \left[ \frac{b}{Y} (s_{n+1}^{\text{trial}} - (1 - D_{n+1}) \alpha_{n+1} - 2\mu n_{n+1} \Delta \gamma) - \beta_n \right] \Delta \gamma \quad (31)$$

$$\Delta\alpha_* = C \begin{bmatrix} \frac{B+R-Y}{Y} (s_{n+1}^{\text{trial}} - (1-D_{n+1})\alpha_{n+1} - 2\mu n_{n+1}\Delta\gamma) \\ -\sqrt{\frac{B+R-Y}{\|\alpha_{*n}\|}} \alpha_{*n} \end{bmatrix} \Delta\gamma \quad (32)$$

$$D_{n+1} = D_n + \left( \frac{\sigma_{di}^c}{G_f} \right) \Delta\gamma \quad (34)$$

$$I_{ddi(n+1)} = I_{ddi(n)} + \frac{\Delta\gamma}{\varepsilon_{ddi(n+1)}^p} \quad (35)$$

$$\Delta R = k(R_{\text{sat}} - R) \Delta\gamma \quad (33)$$

$$I_{df(n+1)} = I_{df(n)} + \frac{\Delta\gamma}{\varepsilon_{df(n+1)}^p - \varepsilon_{ddi(n+1)}^p} \quad (36)$$

Note that since the strength differential effect was weak for DP steels, especially DP980,<sup>[31]</sup> using the von Mises yield surface model was sufficiently accurate. Calculating the damage parameter and assessing the initiation of ductile damage and fracture by using the indicators  $I_{ddi(n+1)}$  and  $I_{df(n+1)}$

The flow potential function could be written based on  $\Delta\gamma$  with the form

$$\Phi_{n+1} = \|A + B\Delta\gamma\| + C + D\Delta\gamma = aa + bb\Delta\gamma + cc + dd\Delta\gamma \quad (37)$$

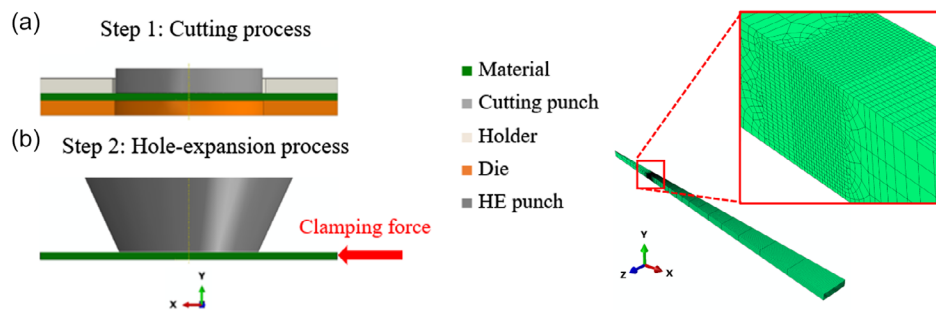


**Figure 4.** The assembly (left) and mesh pattern (right) of the created model.

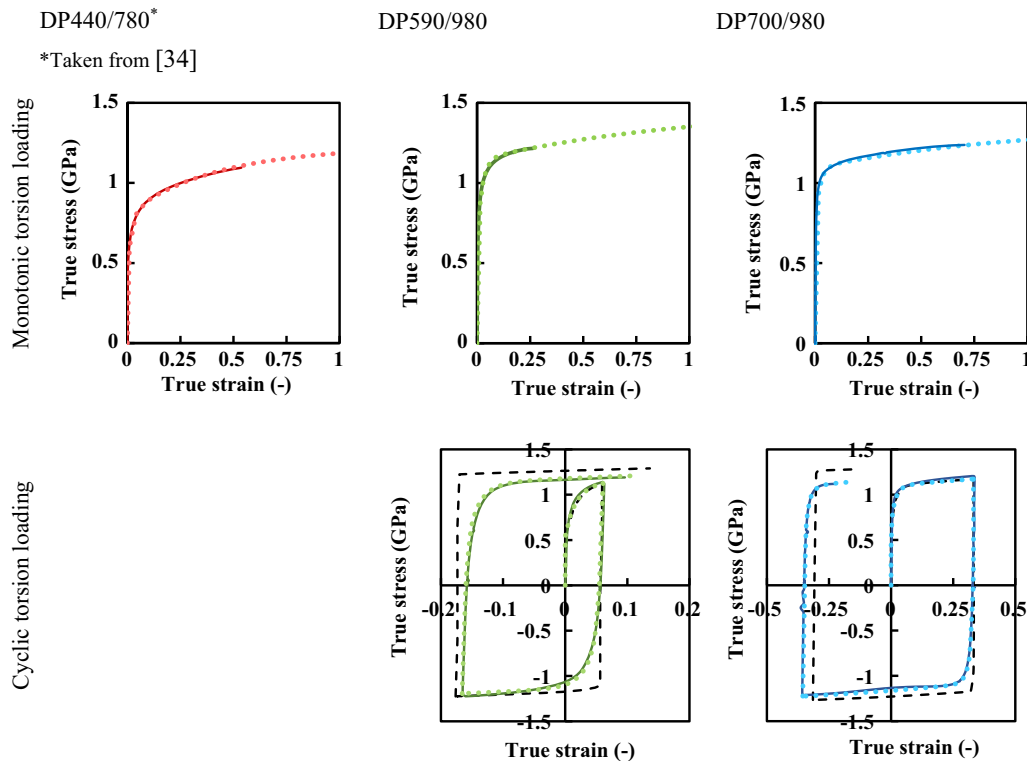


**Figure 5.** Comparison between the flow curves of experiments (solid lines), simulations with YU plasticity (dotted lines), and isotropic hardening (black dashed lines).<sup>[37]</sup>

By assuming  $(\Delta\gamma)^2 \approx 0$  is negligible

$$(\Delta\gamma)^2 \approx 0 \quad (38)$$

The plastic multiplier is calculated as

$$\Delta\gamma = -\frac{aa + cc}{bb + dd} \quad (39)$$

**Table 3.** Calibrated parameters for YU plasticity and the fracture model for the studied materials at reference stress rate ( $\dot{\epsilon}_0^p = 0.001 \text{ s}^{-1}$ ) and temperature ( $T_0 = 298 \text{ K}$ ).

	Y	B	$R_{\text{sat}}$	C	K	b	$D_1$	$D_2$	$D_3$	$D_4$	$D_5$	$D_6$
DP440/780	440	830	190	100	2.4	5	1.20	1.50	0.68	2.43	0.35	0.20
DP590/980	610	1150	157	85	1	5	1.00	2.60	0.41	1.70	0.25	0.00
DP700/980	705	1100	133	100	1	5	2.00	2.20	0.86	1.90	0.41	0.00

With the plastic corrector, deviatoric stress tensor  $s$ , stress tensor  $\sigma$ , and equivalent stress  $\bar{\sigma}$  can be updated backwardly for time  $n + 1$ .

### 2.3.2. Simulation Model

To study and analyze the deformation history and damage evolution of the experiments, parallel FE models were employed using Abaqus 2019/Explicit software. The details of the models were described in the following section.

**Calibration of Models:** The constants of plasticity and damage models were calibrated reversely by comparison of flow curve and force–displacement curves between the simulations and experiments. Since for high-strength DP steels, the fracture happened immediately after damage initiation,<sup>[28,29]</sup> the damage and fracture indicators were defined the same. The eight-node brick elements with reduced integration (C3D8R) and size of  $0.1 \times 0.1 \times 0.1 \text{ mm}^3$  were applied at

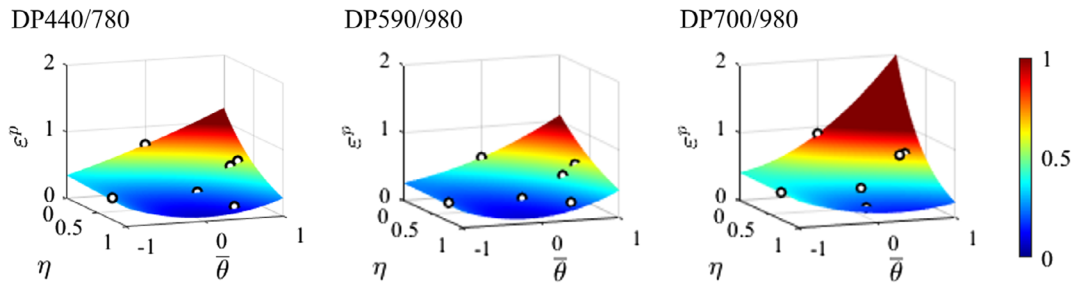


**Figure 6.** Ductile fracture loci of the investigated DP steels.

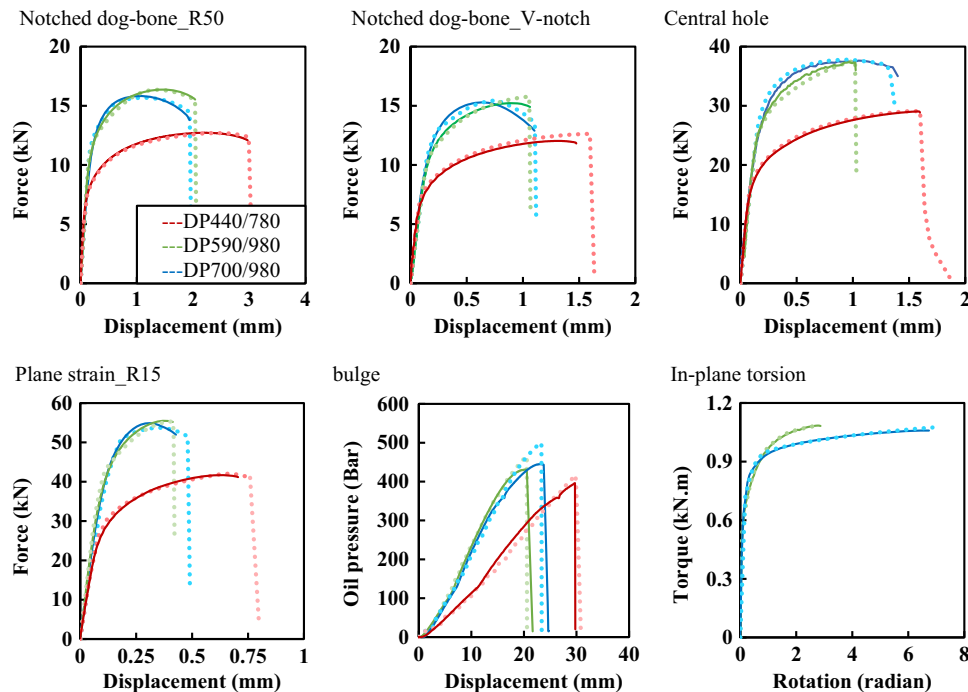


**Figure 7.** Responses of the materials through various testing techniques, experimental results (solid lines), and simulation results (dotted lines). The torsion test was not performed for DP440/780 in this study.

the critical areas, where the deformation and damage concentrated.

**Shear-Cutting and the Subsequent Hole Expansion Processes:** The shear-cutting and the following HET were simulated as a one-stroke two-step model. In this model, the cutting punch, holder, die, and hole-expansion punch were designed as solid rigid parts, while the sheet was a deformable solid. In order to reduce the computational time and according to the symmetric axes, only  $5^\circ$  of setup was studied. The C3D8R elements with a size of  $0.025 \times 0.025 \times 0.025 \text{ mm}^3$  were used in the critical areas to capture relatively accurate damage distribution at the shear-cut edges. However, for the simulation of wire-cut edges, the element size of  $0.1 \times 0.1 \times 0.1 \text{ mm}^3$  was used to decrease the running time. The setup assembly and mesh pattern are depicted in **Figure 4**. The Coulomb friction coefficient of  $0.1^{[32,33]}$  was applied between the contact pairs which were defined by a node-to-surface algorithm. An optimal clamping force was

chosen such that the blank was neither drawn in nor torn improperly during the forming processes.

### 3. Results and Discussion

The capability of the proposed method was assessed for 3 DP steel sheets. At first, the model material parameters were calibrated for each material (Section 3.1) and then the calibrated models were applied for the prediction of various shear-cutting processes (Section 3.2) and HET (Section 3.3).

#### 3.1. Materials Behavior and Calibration

The YU plasticity model was calibrated through monotonic and cyclic torsion loading conditions (**Figure 5** and **Table 3**). The in-plane torsion test induced a shear stress state ( $\eta = 0$ )

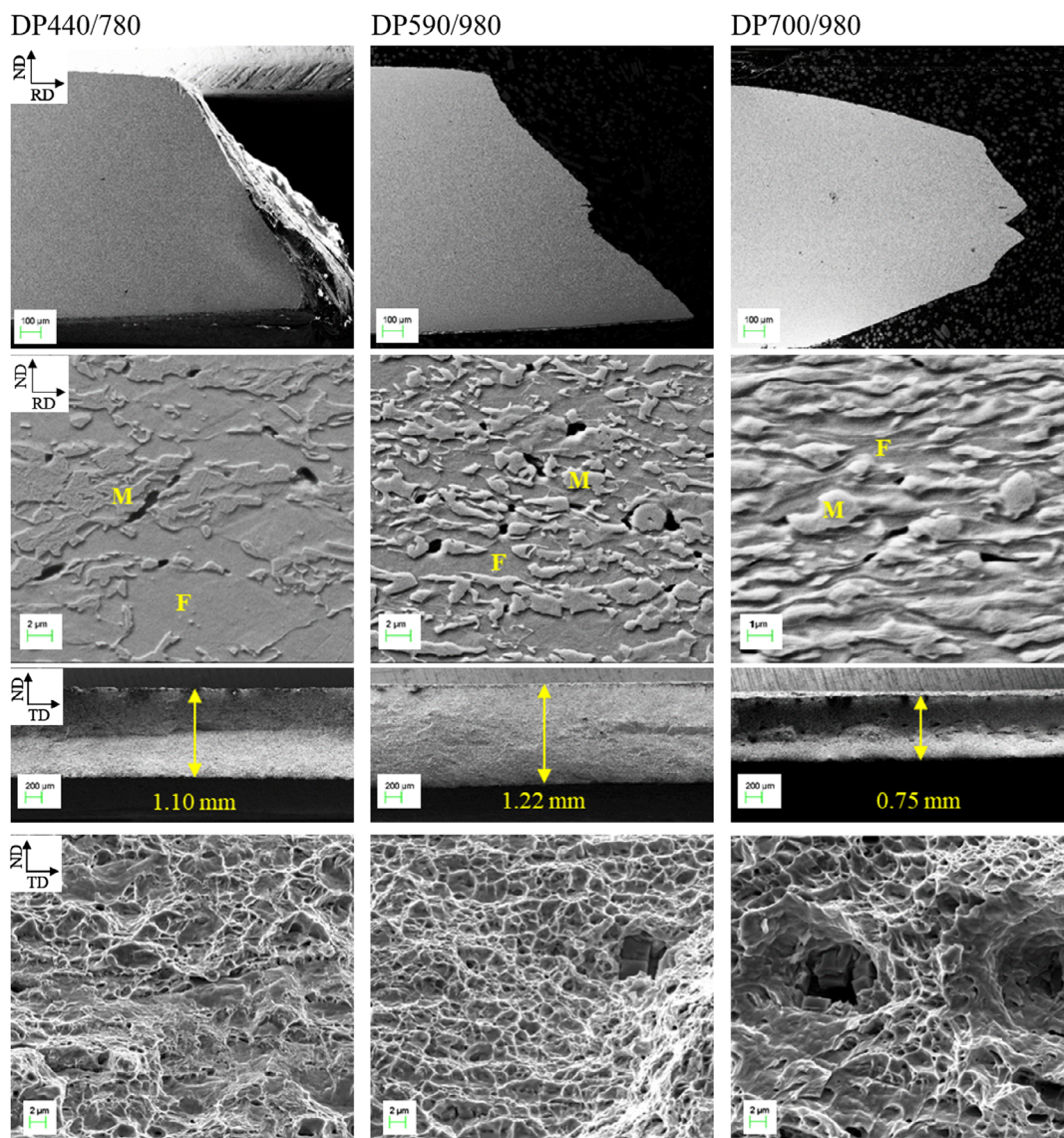


**Figure 8.** SEM micrographs from different views of the fracture site for uniaxial tensile tests.



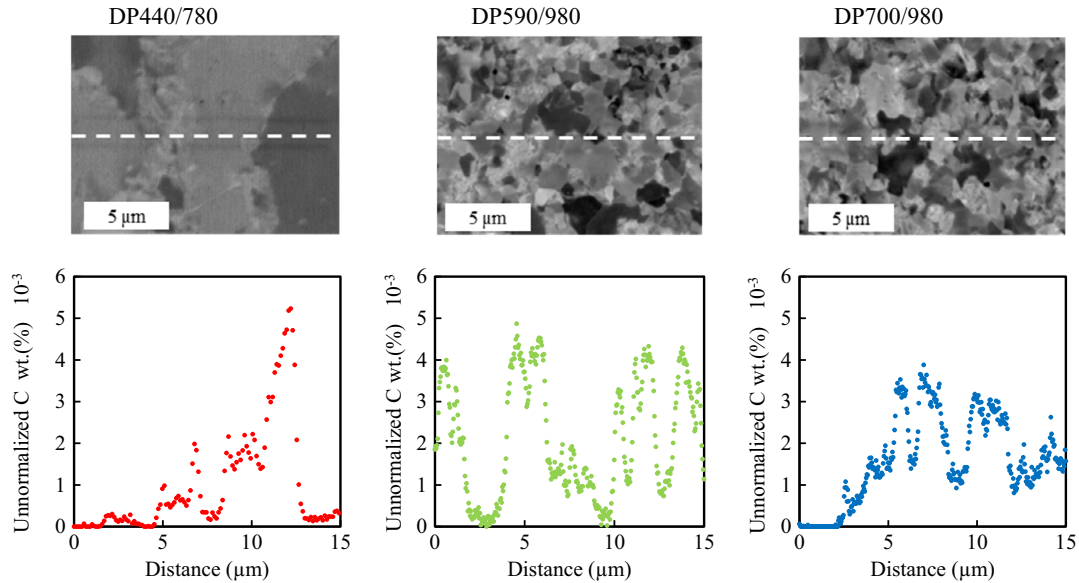


**Figure 9.** The EPMA line scan results for carbon content for each material. The area with zero carbon content represents ferrite grains.

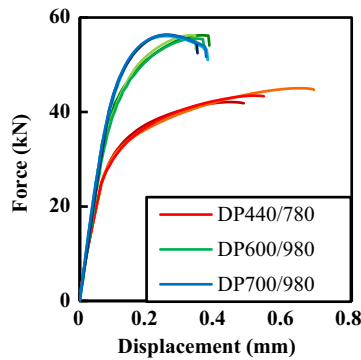


**Figure 10.** Range of scattering data of plane strain with 7.5 mm grooves for different studied materials, which is very large for DP440/780.

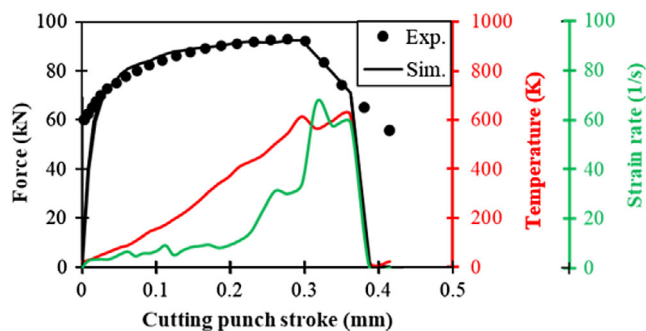


**Figure 11.** Comparison of force–displacement between the experiment and simulation for  $\varnothing_{\text{Cutting die}}$  of 30 mm and clearance of 13%. The maximum temperature and strain rate throughout the cutting were derived from the simulation.

**Table 4.** Calibrated parameters for plasticity correction due to strain rate and plasticity, as well as fracture parameters for shear-cutting loading (as dynamic fracture parameters at  $\dot{\theta} = 0$ ).

	$c_1^{\text{ip}}$	$c_2^{\text{ip}}$	$c_1^{\text{T}}$	$c_2^{\text{T}}$	$c_3^{\text{T}}$	$D_3^{\text{cut}}$	$D_4^{\text{cut}}$
DP590/980	0.01 <sup>b)</sup>	1.092 <sup>a,b)</sup>	2.2 <sup>b)</sup>	0.017 <sup>b)</sup>	1.005 <sup>b)</sup>	0.75	1.60
DP700/980	0.007 <sup>c)</sup>	1.064 <sup>a,c)</sup>	0.62 <sup>c)</sup>	0.005 <sup>c)</sup>	0.86 <sup>c)</sup>	1.19	1.30

<sup>a)</sup>In the current formulation with  $\dot{\epsilon}_0^{\text{p}} = 0.001 \text{ s}^{-1}$  ( $c_2^{\text{ip}} = 1 - c_1^{\text{ip}} \cdot \ln \dot{\epsilon}_0^{\text{p}}$ ); <sup>b)</sup>Taken from the study;<sup>[38]</sup> <sup>c)</sup>Taken from the study.<sup>[29]</sup>

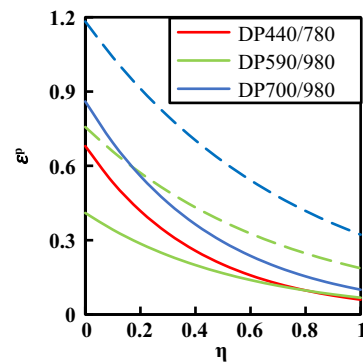


**Figure 12.** Comparison of the calibrated  $D_3$  and  $D_4$  for quasistatic tests (solid lines) and shear-cutting/intermediate speed tests (dashed lines).

with no deformation localization. Thus, the whole flow curves up to fracture were considered for the calibration process. To investigate the advantages of the YU model, the same cyclic loading was also simulated using true stress–strain data of the monotonic loadings along with the default isotropic hardening in Abaqus. These results are shown in Figure 5 in

black dashed lines. Figure 5 reveals the earlier yielding was successfully predicted using YU plasticity, while obviously isotropic hardening approach was unable to. Since fracture behavior occurs shortly after damage in many high-strength DP steels as indicated in some studies,<sup>[28,29]</sup> using an uncoupled fracture model could work properly and even accurately. Therefore, the uncoupled version of the aforementioned damage model was employed. The calibrated parameters are listed in Table 3 and the calculated fracture strains are plotted in the space of stress triaxiality, normalized Lode angle

parameter in Figure 6. The calibrated plasticity-damage model showed the accurate prediction of material response for different stress states (Figure 7). The fracture locus of DP700/980 was significantly higher than others, which implies higher local deformation.

Accordingly, the thickness reduction, damage micromechanisms, and fracture surface of these specimens were observed through the SEM micrographs as each material endured necking differently (Figure 8). The thickness measurement at the central part of the fracture site reveals that the thickness reduced from

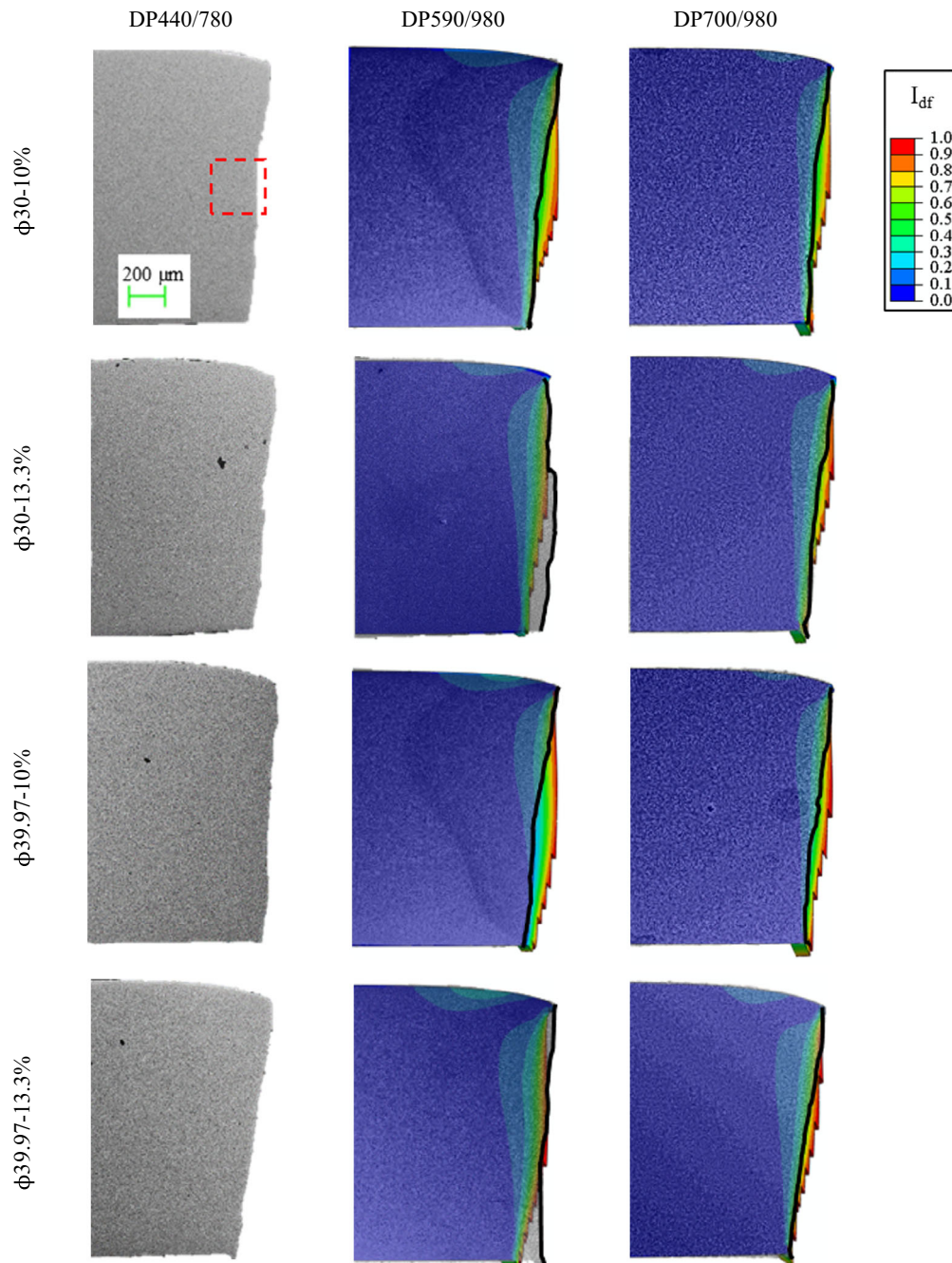


**Figure 13.** Comparison of the cut edge in simulations (colorful pattern of fracture indicator distribution) and experiments (gray background).

1.5 mm to 1.10 mm and 1.22 mm for DP440/780 and DP590/980 by small localization and through-thickness shearing and to 0.75 mm for DP700/980 by severe necking. In addition, distinguished damage micromechanisms were observed for each studied steel. Martensite cracking is the dominant failure mechanism in DP440/780 (mostly in the martensite bands) and DP590/980, while decohesion between ferrite and martensite interfaces is the main damage mechanism for DP700/980. These distinct damage behaviors were dictated by deformation distribution through the material and between the phases, as a result of microstructural features. Phase fractions, their distributions, and morphologies in Figure 1, as well as phase strength differences, which were estimated by the local carbon content in Figure 9, play the main roles. Therefore, it can be briefly concluded that the closer phase fractions, finer grain sizes, phase distribution consistency, and lower strength differences of individual phases led DP700/980

to accommodate the deformation more homogeneously and retard the damage initiation. It is worth mentioning that due to wide martensitic band structures, DP440/780 showed large scatter data for its local formability, which was even more considerable in specific stress states. For example, Figure 10 displays the reproducibility of results for a plane-strain tensile test for the studied DP steels. The three repeats for DP440/780 fractured at a wide range of displacement, which made the numerical study of the failure behavior of this material difficult.

### 3.2. Shear-Cutting

Shear-cutting induces severe hardening and some damage on the edge as well as the adjacent material, which could drastically reduce the edge formability. To describe accurately the SAZ in simulations, the effects of strain rate and generated adiabatic

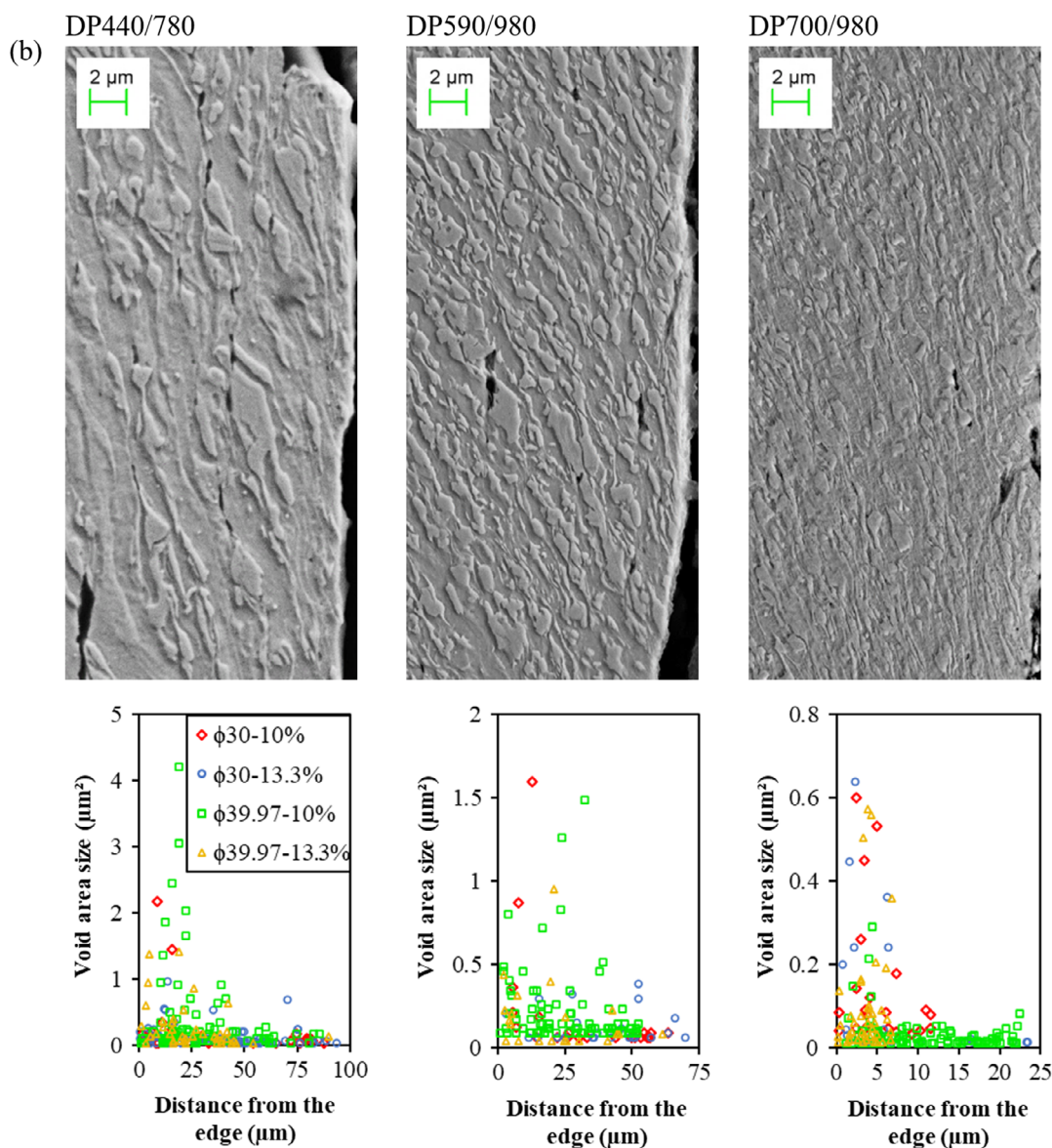


**Figure 14.** Microcrack formation at the shear cut edge for different cutting conditions.



heating were considered in both plasticity and fracture behaviors. The implementation of strain rate and temperature functions into plasticity was explained before, and the calibrated parameters were extracted from previous works for exactly the same DP590/980 and DP700/980 (Table 3). Although the punching speed was  $1 \text{ mm s}^{-1}$ , which is usually not considered a very fast condition, the simulations showed intermediate strain rates in the deformed zone (Figure 11). The strain rate increased gradually from 2 to  $30 \text{ s}^{-1}$  before the crack appeared and afterwards rose to over  $60 \text{ s}^{-1}$ . Consequently, the temperature increased locally up to 450 and 620 K before and right after the crack initiation. Since these loading conditions were different from the tests for calibration of fracture loci, the fracture parameters were recalibrated for shear-cutting using a reverse approach of fitting force–displacement curves. Fortunately, the stress state throughout this process evolves at  $\bar{\theta} \approx 0$ .<sup>[33]</sup> Therefore, only  $D_3$  and  $D_4$  were required to be adjusted (Table 4). The new loci represented higher fracture strains for an intermediate range of strain rates (Figure 12), as expected from previous reports.<sup>[34,35]</sup>

The edge characteristics of different conditions for experimental tests are compared with the simulations in Figure 13. The darker figures with dot patterns show the experiment images with black-marked edges and the colorful patterns represent the simulated ones. The colors indicate the distribution of the fracture indicator. Due to the lack of experimental data, simulations were not performed for DP440/780. According to the results, the

highest amount of damage concentrated at fracture and burr parts of the edge, because the final separations happened also there. The burr sizes are negligible for all cases. The SAZ size was smaller in smaller hole size as well as smaller clearance. Secondary burnishes were observed in the 10% clearance for all the studied steels. As the crack path was not wide enough to let the crack propagate easily, a second crack appeared to accomplish the cutting.<sup>[16]</sup> In this case, usually several microcracks form which create rougher surfaces than relatively larger clearances. Since the applied element size was not sufficiently fine, the simulation edges could not perfectly match the experiments. However, the accumulated hardening and damage play the main role in edge cracking during subsequent forming processes.<sup>[36]</sup>

The size of SAZ was also experimentally investigated by measuring the size and distribution of formed microcracks in an area of  $300 \times 300 \mu\text{m}$  at the middle of the fracture zone which is marked in Figure 13 with a red square. The experimental void distribution is shown in Figure 14. The larger voids were discovered in lower clearances, which implies the difficulties that the main crack has faced with propagating. It therefore needed a secondary crack to occur. Besides cutting tool conditions, the damage behavior of materials is another contributing factor to the size of SAZ. Figure 14 displays the furthest voids from the cut edge which were observed about 90, 75, and  $25 \mu\text{m}$  for DP440/780, DP590/980, and DP700/980, respectively, which

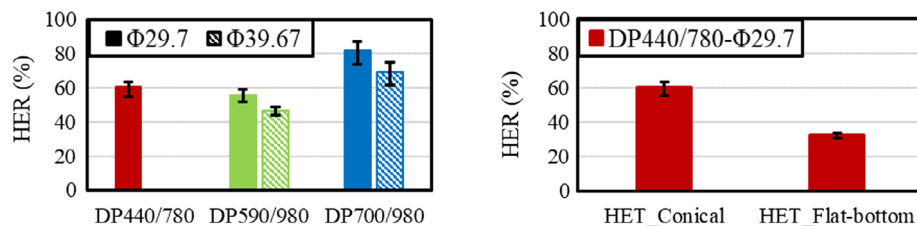


**Figure 15.** The HER of the wire-cut holes for different conditions, (left) for different materials with HET conical punch, and (right) with a hole size of 29.7 with a HET flat-bottom punch.

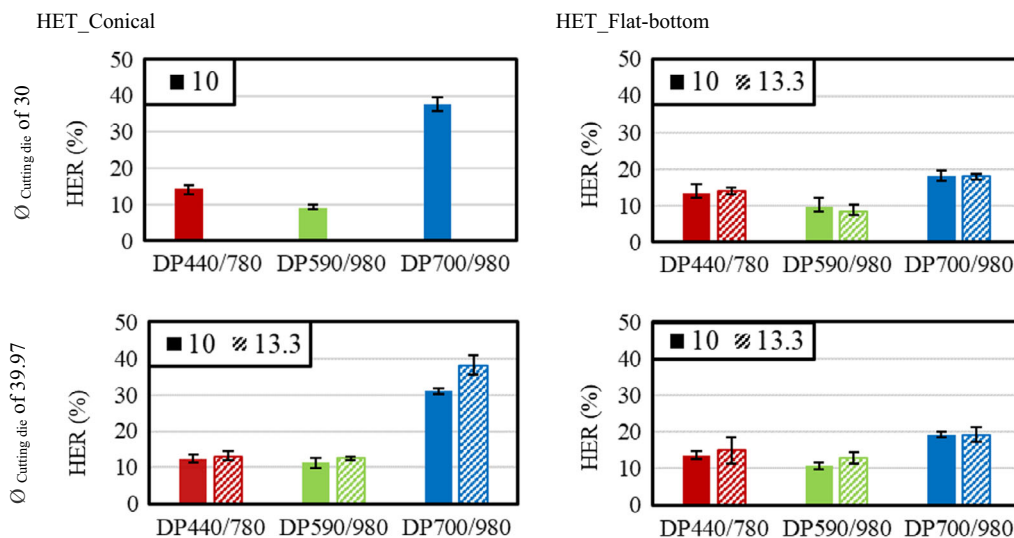


**Figure 16.** Comparison of HER between different materials, cutting conditions, and hole expansion punches.



could indicate the SAZ size for each material. Furthermore, the void sizes were significantly different for each material. The size of the largest observed void was about 4.2, 1.6, and 0.65  $\mu\text{m}$  for DP440/780, DP590/980, and DP700/980, respectively. Note that the microcracks around the inclusions were not considered. This trend is expected as each steel endured deformation and fracturing differently, as discussed in the previous section. Also, the numerical fracture distribution in Figure 13 illustrates a smaller SAZ for DP700/980.

### 3.3. HET

The HET were also performed on both the wire-cut edges and shear-cut edges, by using conical as well as flat-bottom punches. This test is massively employed as a simulative test to quantify the edge crack sensitivity by offering the HER parameter. However, because of differing setup and forming parameters, the standard HER needs to be reconsidered and it cannot be directly used in production procedures. For instance, according

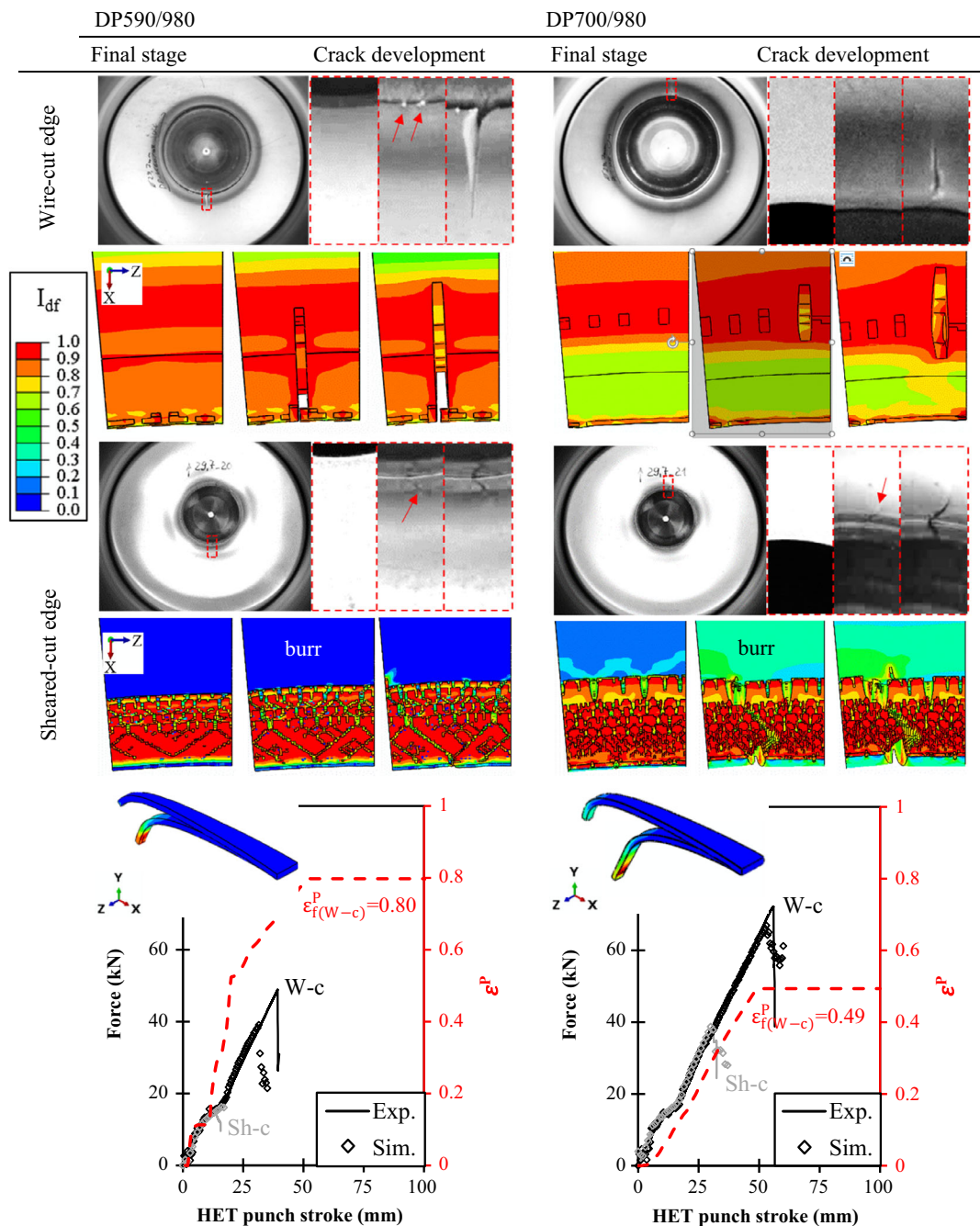


**Figure 17.** Comparison of damage evolution during HET between wire-cut and sheared-cut edges. The initial hole size is 29.7 mm. Also, the plastic strain changes history for the critical elements throughout the HET are plotted.

to the definition of HER (Equation (40)), decreasing the initial hole size ( $D_0$ ) could increase the HER, which does not necessarily imply that the forming limits are higher in the specific condition.  $D_h$  is the average hole diameter after rupture during HET. Hence, the HER values are only comparable within one set of tool conditions.

$$HER = \frac{D_h - D_0}{D_0} \times 100 = \left( \frac{D_h}{D_0} - 1 \right) \times 100 \quad (40)$$

The conventional HER was calculated for each case and is plotted in **Figure 15** and **16**. The key findings are summarized as follows: 1) DP700/980 represented notably higher HERs. HERs for DP440/780 are slightly higher than DP590/980. These responses were predictable based on the different damage behavior of the studied materials; 2) The shear-cutting reduced the edge flangeability to even one-quarter in comparison to the wire-cutting technique; 3) Applying the higher clearance (13.3%) might cause higher HER. Forming of the secondary burnished part and more microcracks in clearance of 10% led to a rougher surface and lower edge quality; and 4) The HET flat-bottom punch could decrease HER significantly, and in the case of

DP700/980, HER remained constant, regardless of edge condition.

These phenomena are discussed more elaborately below, assisted by simulation outcomes. Besides employing accurate material modeling and inputs, considering the loading history is crucial in the simulation of complex forming processes. This approach provides in-depth information on the failure happenings.

**Figure 17** shows the damage evolution during the HET with a conical punch for four specimens, a combination of two materials (DP590/980 and DP700/980) and two hole-manufacturing processes (wire-cutting or shear-cutting). The initial hole size was 29.7 mm for all the specimens in this figure. It demonstrates good agreement between the simulations and experiments in terms of the force–displacement response and crack initiation site. Since the shear-cut edges underwent higher prior damage, their HE forces dropped significantly earlier than the wire-cut edges. However, it was not the only effect of predamage. **Figure 17** reveals the crack site also altered and edge cracking was promoted. In other words, for wire-cut edges during the HET, cracks were initiated for DP590/980 at the edge inner corner (next to the HET punch) and for DP700/980 a bit away from the edge. In contrast, it happened at the outer corner of

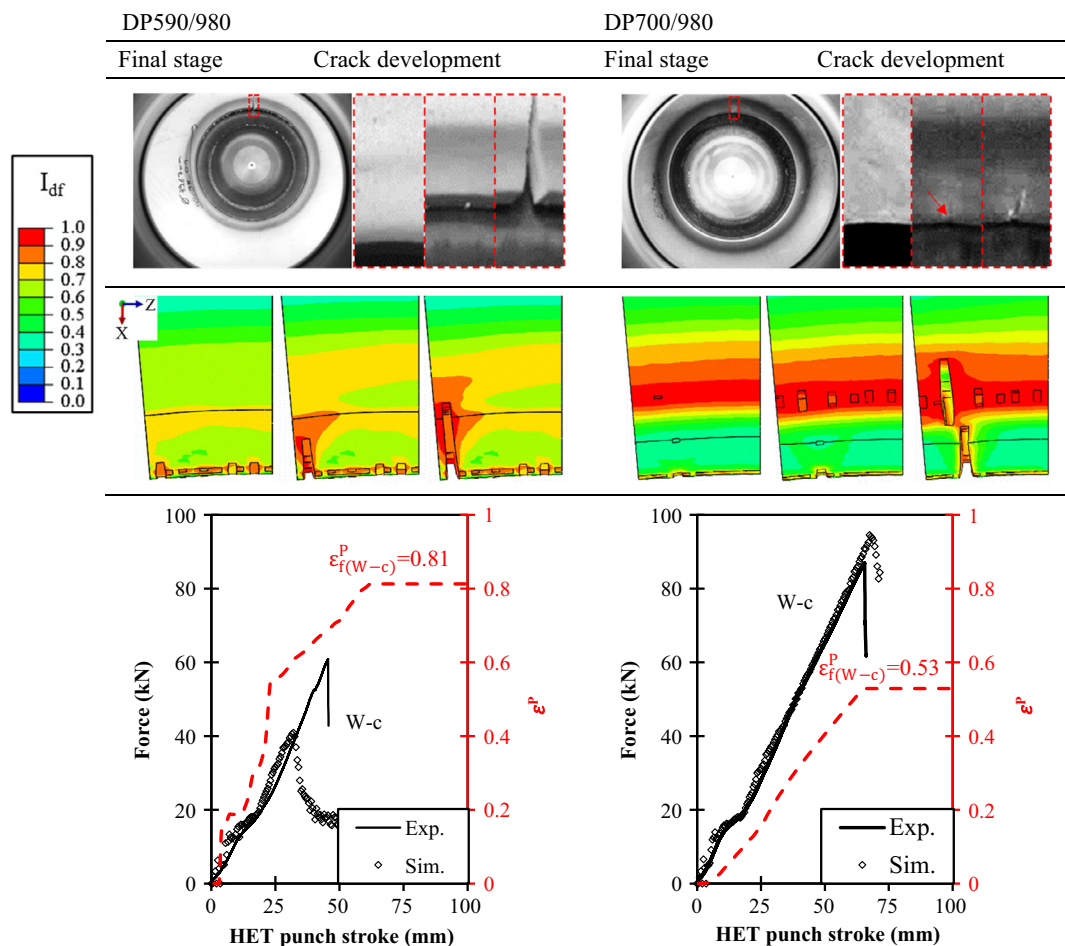


**Figure 18.** Crack evolution for wire-cut edges of hole size 39.67 mm.

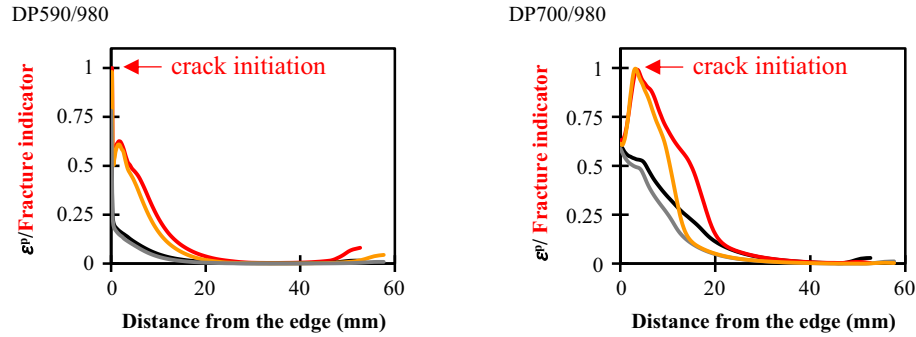


**Figure 19.** Gradients of strain and fracture indicator for wire-cut holes with different initial sizes, 29.7 mm (lighter colors) and 39.67 mm (darker colors).

sheared-cut edges for both materials, where the burr parts with higher residual damage were located.

The crack initiation site could vary also for different initial hole sizes. **Figure 18** shows the results for the wire-cut hole with an initial size of 39.67 mm. For DP700/980, the final crack formed by the initiation of two cracks, from the inner edge like DP590/980, and the other far from the edge. The comparison of force-displacement between different hole sizes (Figure 17 and 18) shows the failure happened earlier for the smaller hole size, although the measured HERs are higher for them in Figure 16. Nevertheless, the derived fracture strains from the

first deleted elements were very close, which signifies the formability was not affected by the size of the hole. As suggested in the previous works,<sup>[19,20]</sup> a larger strain gradient leads to a delay in localization and exceeds the forming limits. Therefore, the equivalent plastic strains and fracture indicators ( $I_{df}$ ) were plotted regarding the distance in the radial direction at the frame that a crack initiated (**Figure 19**). When the value of  $I_{df}$  reaches the threshold of one, the element is deleted. Surprisingly, the results reveal that the cracks initiated from the same distance from the manufactured edges. In other words, for DP590/980, the crack initiated from the edge likewise the smaller hole.

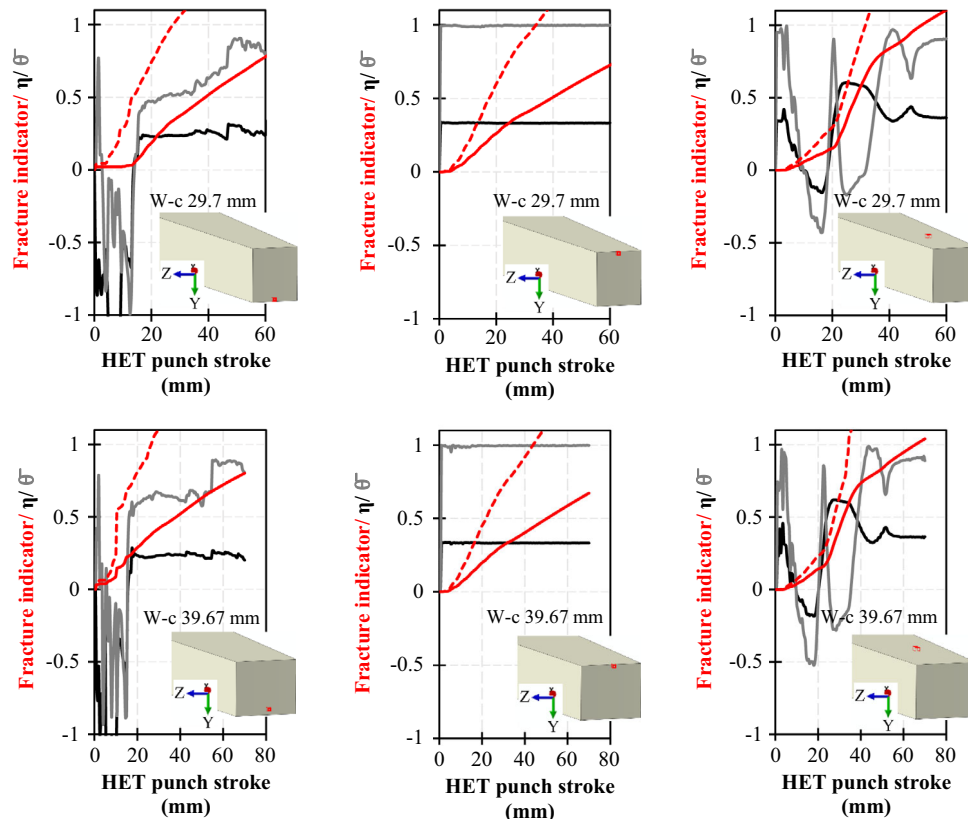


**Figure 20.** Comparison of stress state and damage evolution for the critical elements during conical HET for DP590/980 (red dashed line) and DP700/980 (red solid line) between the wire-cut holes with sizes of 29.7 mm (first row) and 39.67 mm (second row). Note that the stress states for the same elements but different materials are almost identical here.

For DP700/980, the failure initiated with a plane-strain necking far from the edge, which triggered the cracking similar to the smaller hole. However, in addition, some edge cracks appeared and were connected to the former one. To disclose the loading conditions of critical sites for each specimen, the stress states were extracted for different elements in terms of stress triaxiality and normalized Lode angle parameter. Also, the damage behavior of the studied materials for each element is displayed in **Figure 20**, with respect to fracture indicator evolution. It seems the stress state histories are approximately identical for both hole sizes, only proportionally shrank/extended regarding the failure time (= force drop displacement). The steep slope of damage evolution in DP590/980 versus DP700/980 recalls the significant difference in the levels of their fracture strains. Based on the extracted damage evolution, for DP590/980, the edge elements failed earlier than the ones at the contact site with the HET punch. In contrast, for DP700/980, the elements at the contact site met  $I_{df}=1$  faster than the edge elements. According to the results, it can be roughly concluded that the crack initiation site is dictated by fracture strain differences between  $\eta \approx 0.33$ ,  $\bar{\theta} \approx 1.00$  and  $\eta \approx 0.6$ ,  $\bar{\theta} \approx -0.25$ . In case the former is not sufficiently higher than the latter, the probability of edge cracking increases.

Additionally, the shape of the HET punch diversifies damage evolution in the specimens. Although the HER values were

strongly diminished in comparison to the results of the conical punch, the formability was only material dependent and remained constant, while only the employed stress states were different. As a reminder, HER values are not comparable for different HET setups. The comparison of crack initiation sites between the sheared-cut and wire-cut edges for DP440/980 shows two critical locations are prone to cracking. One is at the edge and the other one is in the middle of the punch contact area (**Figure 21**). In case the accumulated damage from the edge manufacturing step is high enough, the crack appears at the edge, which is counted as the edge cracking category. Otherwise, the crack initiates far from the edge. Therefore, edge cracking was observed for DP440/980 with the sheared-cut edge, while plane-strain localization occurred in the specimen with the wire-cut edge.

Although the HER values for DP440/780 and DP590/980 were slightly different for different sheared-cut edge conditions with HET flat-bottom punches, they remained constant for DP700/980. In fact for this material, although some small cracks were observed at the edge, the main failure was not due to edge cracking (**Figure 22**). Therefore, the crack sensitivity was not influenced by the edge quality. Tracking the stress state and damage evolution for shear-cut edges during applying the HET flat-bottom punch (**Figure 23**) shows the uniaxial tension loading ( $\eta \approx 0.33$ ,  $\bar{\theta} \approx 1.00$ ) at the edge and the stress state of

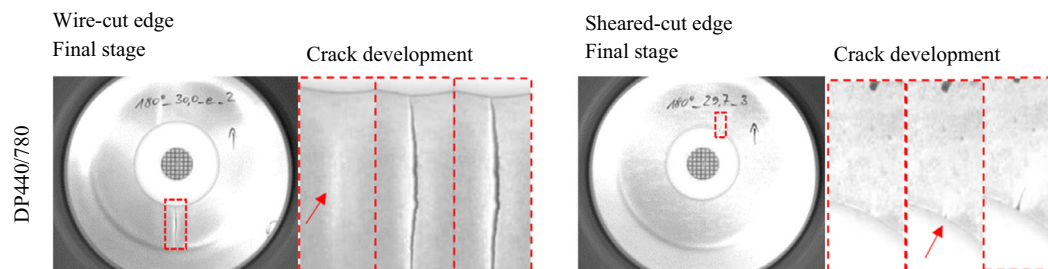


**Figure 21.** Crack initiation and propagation during hole expansion of DP440/980 with the flat-bottom punch for wire-cut and sheared-cut holes with a size of 29.7 mm.

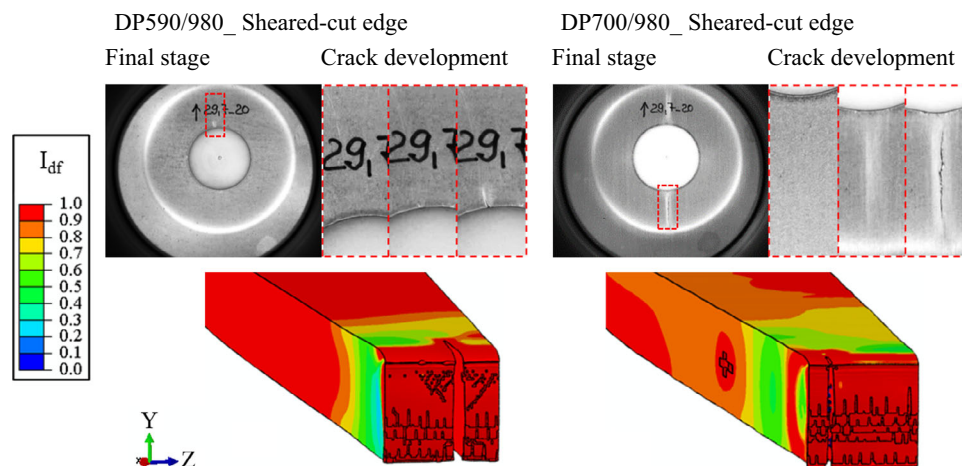


**Figure 22.** Crack initiation and propagation during hole expansion with the flat-bottom punch for sheared-cut holes with the size of 29.7 mm. The simulations are taken from the force drop frame.



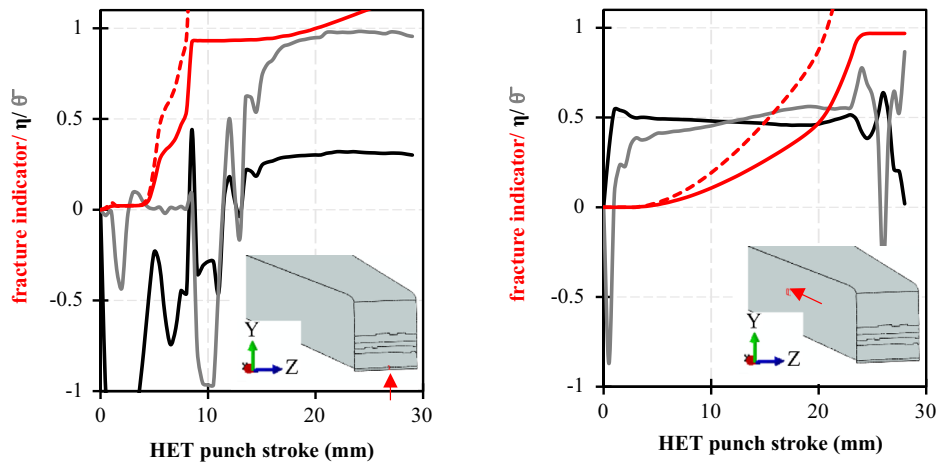


**Figure 23.** Comparison of stress state and damage evolution during flat-bottom HET for the critical elements between DP590/980 (red dashed line) and DP700/980 (red solid line) for the sheared-cut holes with a size of 29.7 mm. Note that the stress states for the same elements but different materials are almost identical here.

$\eta \approx 0.5$ ,  $\bar{\epsilon} \approx 0.5$  through the contact area with the punch. The results reveal that the deformation at the edge for DP590/980 is highly sensitive to cracking. Therefore, this material is more sensitive to the effects of edge quality. It should be mentioned that despite the crack sites being predicted correctly for DP700/980 in the simulations with HET flat-bottom punch, the force drop displacements were quite late, and the predicted HERs were almost double the experimental results. This problem could be solved by defining a much lower fracture strain for  $\eta \approx 0.5$ ,  $\bar{\epsilon} \approx 0.5$  versus  $\eta \approx 0.33$ ,  $\bar{\epsilon} \approx 1.00$ . Unfortunately, it is not feasible considering the equation of fracture strains and experimental results for the calibration. In brief, edge manufacturing and further edge forming do not change the intrinsic formability of materials. Only the accumulated damage should be considered throughout the entire production process, which could be easier and more accurate with a proper computer-aided method, since some DP steels could show high local formability which is not obvious from the experimental assessment of their global formability.

#### 4. Conclusion

This study introduces a groundbreaking approach to investigating edge cracking in multistep forming processes, addressing a gap in traditional experimental methods like HET, which have proven unreliable for evaluating edge crack sensitivity in manufacturing. By employing FE methods in computer-aided engineering, this research provides a powerful tool for accurately predicting mechanical and failure behaviors of the materials throughout the complex forming processes. The novelty lies in the incorporation of precise material models, such as the YU isotropic-kinematic hardening model coupled with the BW fracture model, which are essential for designing complex forming processes. Additionally, the influence of strain rate, adiabatic heating, and the Bauschinger effect were taken into the account. According to the results, the following conclusions can be drawn: 1) The microstructural features impose the

deformation distribution throughout the material and facilitate/retard the failure. In brief, a material with more homogeneous microstructural and micromechanical characteristics represents higher local formability limits. In this work, the void sizes and their distribution throughout the SAZ area as well as the standard HER illustrated approved the important role of microstructure on the damage behavior; 2) The YU isotropic-kinematic hardening model coupled with the BW fracture model is a promising approach for designing a complex multistep forming process. However, it requires cyclic loading for calibration of the YU model and at least 6 different stress states for calibration of BW. The suggested testing techniques in this work satisfied all the requirements; 3) In case of rapid fracture after damage initiation, like for studied DP steels, the uncoupled fracture version could still show high accuracy; 4) The effects of strain rate and induced adiabatic heating were also considered. Although the speed of the cutting process was quite low ( $1 \text{ mm s}^{-1}$ ), high strain rates of up to  $60 \text{ mm s}^{-1}$  were observed in the deformed zone, which generated temperatures up to 620 K at the end. Therefore, using the fracture loci for quasistatic conditions was not feasible, and a second fracture locus was proposed through the shear-cutting process; 5) Failure through HE tests is affected by the setup design besides the edge quality; and 6) Cracking happens when the accumulated damage reaches its threshold, whether at the edge or far from it. Therefore, a comprehensive tool, like the computer-aided method, is required to consider the evolution of the whole component throughout the entire process.

#### Acknowledgements

The authors gratefully acknowledge Dr. Heinrich Traphöner from TU Dortmund for performing in-plane torsion tests. Thanks to Barbara Hoppe for her support in the material modeling script. In addition, the simulations were performed with computing resources granted by RWTH Aachen University under project <rwth0459> and <rwth1234>. Open Access funding enabled and organized by Projekt DEAL.

## Conflict of Interest

The authors declare no conflict of interest.

## Author Contributions

**Niloufar Habibi:** Writing the Original Draft, Methodology, Data Curation, Investigation, and Software; **Thorsten Beier:** Resource and Investigation; **Junhe Lian:** Writing the Review and Editing; **Berk Tekkaya:** Writing the Review and Editing; **Markus Koenemann:** Supervision; **Sebastian Muenstermann:** Supervision, Funding Acquisition, and Writing the Review and Editing.

## Data Availability Statement

The data that support the findings of this study are available from the corresponding author upon reasonable request.

## Keywords

dual-phase steels, edge crack sensitivity, finite element methods, fracture models, kinematic hardening

Received: February 29, 2024

Revised: July 18, 2024

Published online:

- [1] C. C. Tasan, M. Diehl, D. Yan, M. Bechtold, F. Roters, L. Schemmann, C. Zheng, N. Peranio, D. Ponge, M. Koyama, *Annu. Rev. Mater. Res.* **2015**, 45, 391.
- [2] D. Raabe, B. Sun, A. Da Kwiatkowski Silva, B. Gault, H.-W. Yen, K. Sedighiani, P. Thoudend Sukumar, I. R. Souza Filho, S. Katnagallu, E. Jägle, *Metall. Mater. Trans. A* **2020**, 51, 5517.
- [3] D. Casellas, A. Lara, D. Frómeta, D. Gutiérrez, S. Molas, L. Pérez, J. Rehrl, C. Suppan, *Metall. Mater. Trans. A* **2017**, 48, 86.
- [4] S. Heibel, T. Dettinger, W. Nester, T. Clausmeyer, A. E. Tekkaya, *Materials* **2018**, 11, 761.
- [5] M. Schneider, A. Geffert, I. Peshekhodov, A. Bouguecha, B.-A. Behrens, *Mater. Werkstofftech.* **2015**, 46, 1196.
- [6] N. Pathak, C. Butcher, M. J. Worswick, E. Bellhouse, J. Gao, *Materials* **2017**, 10, 346.
- [7] X. Hu, X. Sun, K. Raghavan, R. J. Comstock, Y. Ren, *Mater. Sci. Eng. A* **2020**, 780, 139176.
- [8] N. Habibi, S. Mathi, T. Beier, M. Koenemann, S. Muenstermann, *Crystals* **2022**, 12, 845.
- [9] W. Cho, B.-S. Jeong, K. Jeong, S.-H. Lee, H. Kim, J. Lee, S.-I. Kim, H. N. Han, *J. Mater. Res. Technol.* **2023**, 26, 837.
- [10] N. Habibi, N. Vajragupta, S. Muenstermann, *Crystals* **2021**, 11, 805.
- [11] S. Park, J. Jung, W. Cho, B.-S. Jeong, H. Na, S.-I. Kim, M.-G. Lee, H. N. Han, *Int. J. Plast.* **2021**, 136, 102900.
- [12] K. Wang, M. Luo, T. Wierzbicki, *Int. J. Fract.* **2014**, 187, 245.
- [13] A. Ishiwatari, U. Masaki, T. Inazumi, *JFE Tech. Rep.* **2013**, 18, 96.
- [14] X. H. Hu, X. Sun, S. F. Golovashchenko, *Finite Elem. Anal. Des.* **2016**, 109, 1.
- [15] P. Larour, J. Hinterdorfer, L. Wagner, J. Freudenthaler, A. Grünsteidl, M. Kerschbaum, *IOP Conf. Ser.: Mater. Sci. Eng.* **2022**, 1238, 012041.
- [16] X. Wu, H. Bahmanpour, K. Schmid, *J. Mater. Process. Technol.* **2012**, 212, 1209.
- [17] S. Han, Y. Chang, C. Y. Wang, H. Dong, *J. Mater. Process. Technol.* **2022**, 299, 117377.
- [18] S. K. Paul, *Materialia* **2020**, 9, 100566.
- [19] C. Krempaszky, P. Larour, J. Freudenthaler, E. Werner, in *IDDRG 2014 Conf.*, Paris, France **2014**.
- [20] E. Iizuka, M. Urabe, Y. Yamasaki, Y. Hiramoto, *J. Phys.: Conf. Ser.* **2017**, 896, 012008.
- [21] Q. Yin, A. E. Tekkaya, H. Traphöner, *CIRP Ann.* **2015**, 64, 261.
- [22] W. S. Farren, G. I. Taylor, *Proc. R. Soc. London, Ser. A* **1925**, 107, 422.
- [23] ISO 16630, in *Metallic Materials—Sheet and Strip—Hole Expanding Test*, ISO, Geneva **2017**.
- [24] G. I. Taylor, H. Quinney, *Proc. R. Soc. London, Ser. A* **1934**, 143, 307.
- [25] F. Yoshida, T. Uemori, *Int. J. Plast.* **2002**, 18, 661.
- [26] Y. Bai, T. Wierzbicki, *Int. J. Plast.* **2008**, 24, 1071.
- [27] J. Lian, M. Sharaf, F. Archie, S. Muenstermann, *Int. J. Damage Mech.* **2013**, 22, 188.
- [28] F. Pütz, F. Shen, M. Koenemann, S. Muenstermann, *Int. J. Fract.* **2020**, 226, 1.
- [29] W. Liu, J. Lian, S. Muenstermann, C. Zeng, X. Fang, *Int. J. Mech. Sci.* **2020**, 176, 105534.
- [30] N. Park, H. Huh, S. J. Lim, Y. Lou, Y. S. Kang, M. H. Seo, *Int. J. Plast.* **2017**, 96, 1.
- [31] Y. Hou, J. Min, N. Guo, J. Lin, J. E. Carsley, T. B. Stoughton, H. Traphöner, T. Clausmeyer, A. E. Tekkaya, *J. Mater. Process. Technol.* **2021**, 287, 116314.
- [32] K. Wang, L. Greve, T. Wierzbicki, *Int. J. Solids Struct.* **2015**, 71, 206.
- [33] N. Habibi, M. Zhou, J. Lian, M. Koenemann, S. Muenstermann, *J. Mater. Process. Technol.* **2023**, 316, 117965.
- [34] S. Chandran, W. Liu, J. Lian, S. Muenstermann, P. Verleysen, *Eur. J. Mech., A* **2022**, 92, 104446.
- [35] I. Pätzold, J. Stahl, R. Golle, W. Volk, *J. Mater. Process. Technol.* **2023**, 313, 117872.
- [36] N. Habibi, T. Beier, H. Richter, M. Koenemann, S. Muenstermann, *IOP Conf. Ser.: Mater. Sci. Eng.* **2019**, 651, 012073.
- [37] F. Kolpak, H. Traphöner, O. Hering, A. E. Tekkaya, *CIRP Ann.* **2021**, 70, 247.
- [38] M. J. Koenemann, in *Fakultät für Georessourcen und Materialtechnik der Rheinisch-Westfälischen Technischen Hochschule, RWTH Aachen*, Aachen **2021**.